Analytical calculations for impurity seeded partially detached divertor conditions

A. Kallenbach[1], M. Bernert[1], R. Dux[1], F. Reimold[2], M. Wischmeier[1], ASDEX Upgrade Team

[1]Max Planck Institute for Plasma Physics, D-85748 Garching, Germany
[2]Forschungszentrum Jülich GmbH, Institut für Energie- und Klimaforschung-Plasmaphysik, 52425 Jülich, Germany

Abstract. A simple analytical formula for the impurity seeded partially detached divertor operational point has been developed using 1D modelling. The inclusion of charge exchange momentum loss terms improves the 1D modelling for ASDEX Upgrade conditions and its extrapolation to larger devices. The investigations are concentrated around a partially detached divertor working point of low heat flux and an electron temperature around 2.5 eV at the target which are required to maintain low sputtering rates at a tungsten target plate. An experimental formula for the onset of detachment by nitrogen seeding in ASDEX Upgrade is well reproduced, and predictions are given for N, Ne and Ar seeding for variable device size. Moderate deviations from a linear P_{sep}/R size dependence of the detachment threshold are seen in the modelling caused by upstream radiation at longer field line lengths. The presented formula allows the prediction of the neutral gas or seed impurity pressure which is required to achieve partial detachment for a given P_{sep} in devices with a closed divertor similar to the geometry in ASDEX Upgrade.

1. Introduction

Divertor radiation by seed impurities is required for the necessary spreading of the power to a larger divertor surface area and the achievement of partially detached conditions in devices with high power flux like ITER or DEMO. Species suitable for radiative divertor cooling have to be non-sticking and chemically inactive, primary candidates are argon, neon and nitrogen, provided the chemistry involved for the latter is regarded acceptable for tritium handling. 2D modelling of corresponding divertor conditions makes steady progress, but still has not reached a fully quantitative status for detached conditions [1] [2] [3] [4] [5]. In order to provide simple, but as-reliable-as-possible predictive scalings for future devices simple one-dimensional (1D) model calculations are combined with experimental results from the ASDEX Upgrade (AUG) tokamak.

In this paper, a 1D analytical model is presented which allows the discussion of the major parameter dependencies, provides simple extrapolation towards larger machine sizes and is suitable for incorporation in DEMO design codes or advanced controllers. The major extension regarding previous work is the inclusion of momentum loss processes, which allows the simulation of inter-ELM partially detached divertor conditions. The divertor plasma is approximated by a 1D model representing a flux bundle with the width λ_{int} [6] [7]. Momentum losses and ionization sources are introduced with a simple model, which includes an approximation for the related heat flux dissipation. The goal of this refinement is to provide a better description of the plasma parameters along the flux tube, resulting in a more realistic prediction of the radiation distribution. The model allows quick parameter scans and thus radiation predictions for several impurity species and experimental conditions.

Radiation in the divertor region appears, in a rough approximation, in three locations, namely the outer and inner divertor and the X-point region [8] [9]. A 1D model approach for describing the inner divertor appears not feasible. This is due to the fact that strong detachment is observed here as well as high density regions which cannot be reproduced even by 2-D modelling [4]. In addition, the inner divertor plasma conditions depend sensitively on drifts [10], and poloidally localized transport may be active which is related to the dynamics of the high field side high density region [11]. Radiation from the low field side scrape-off layer (SOL) around the X-point, which is related to the large flux expansion in this region may still be approximated by 1D modelling, while X-point radiation from closed flux surfaces occuring during pronounced detachment requires a different treatment including perpendicular transport and a 2D model which is beyond the scope of this paper. Ideally, model predictions should be directly compared to spatially resolved radiation profiles in the divertor. However, this is not easily obtained due to the insufficient spatial resolution of bolometry, not allowing to disentangle the radiation distribution along a flux bundle. The tomographic grid resolution of AUG bolometry is 3 cm, determined by line-of-sight geometry [12] and viewing cone widths, and thus much wider compared to λ_{int} or parallel gradients close to the plate.

The situation is even more complicated by the occurrence of fast, time dependent radiation phenomena caused by ELMs [12] and divertor fluctuations [13]. To relax these problems, this study concentrates on the working point of partially detached divertor conditions. The non-coronal radiation parameter [14], which influences the radiative efficiency of an impurity species, is set to a value which allows to reproduce the detachment onset of nitrogen seeded AUG discharges.

Partially detached conditions, which mean detachment of the first few power widths on the SOL side of the strike point, are routinely observed in AUG with impurity seeding and also foreseen for ITER [15]. For a future DEMO [16] with tungsten plasma facing components, a low plasma temperature ($T_{i,e}$ below about 5 eV) at the target is not only required for keeping the power load acceptable, but also for limiting the tungsten erosion rate due to impurity sputtering [17] [14] [3]. More pronounced detachment over several power widths [18] [9], which may be an attractive DEMO scenario, is beyond the applicability of 1D modelling, but experimentally found not far above the seeding level which is required for the achievement of partial detachment.

This paper is organized as follows. We start with an introduction of the 1D model used, which mainly follows [19]. The treatment of momentum losses and the boundary conditions at the target have been adapted to provide a good interface to experimental data. The model results are matched against experimental data from ASDEX Upgrade. Finally, a simple formula is presented which relates the neutral pressures of deuterium, the seeding species concentration and P_{sep}/R at the operational point of a partially detached outer divertor.

2. 1D SOL model with momentum loss processes

The divertor plasma conditions and radiative losses are calculated self-consistently using a 1D model representing the region of the first e-folding length of the heat flux outside the separatrix [20] [21] [19] [17]. A flux bundle of length L carrying a heat flux connects the mid-plane with the divertor target. Its cross section is given by the toroidal circumference $\propto$R, the midplane power width λ_q [6], [22], and the field line pitch factor as given in equation 1. The geometry is sketched in figure 1. Atomic data for hydrogen ionization, radiation, charge exchange (CX) and impurity radiation loss are taken from collisional-radiative modelling in ADAS [23]. Hydrogen ionization and radiation are evaluated including their electron density dependence, an overview is given in figure 2. The impurity radiative loss function takes into account non-coronal effects, but no electron density variation is taken into account. Rates have been calculated for a fixed electron density of 10^{20} m^{-3}, which is a very typical value for the divertor SOL. Non-coronal enhancement [24] [14] to radiation is approximated by setting the non-coronal parameter $n_e \cdot \tau = 0.5$ ms $\cdot$ 10^{20} m^{-3}, which allows the reproduction of the onset of N radiation induced detachment in AUG. The residence time τ cannot be accurately specified, but there are trends which limit the variation range of the product $n_e \cdot \tau$. Close to the target plate, the residence time will be far below a millisecond due to

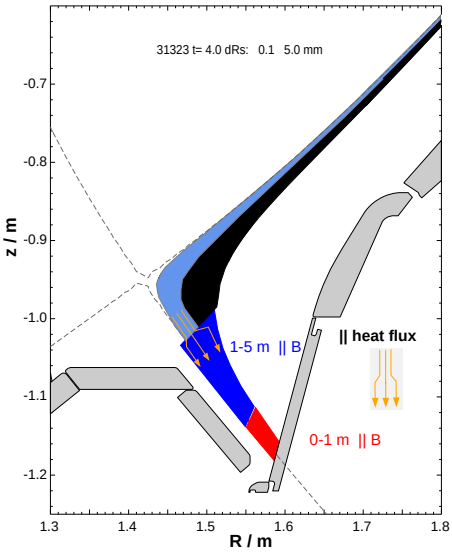

Figure 1. *Geometry of the flux bundle of the 1D model approach in the tokamak. Indicated are the first meter field line length from the target (red color) and meter 1-5 (blue). The X-point height is reached at a distance of 12 m from the target close to the separatrix (0.1 mm outside in the outer midplane) and 7 m at a distance λ_{int} further outside. This distortion cannot be implemented in the 1D model, but it is much less pronounced in the lower outer divertor. The broadening from λ_q to λ_{int} is indicated by arrows. Due to the projected cross section, this is distorted by the changing inclination of the field lines. The parallel heat flux is just assumed to widen instantaneously, as indicated in the inlet. Connection length from target to midplane is about 20 m in the flux bundle at q_{95}= 4.3 in ASDEX Upgrade.*

back-streaming to the target, at densities above 10^{20} m^{-3}. Since T_e is quite low close to the target for the partially detached conditions considered here, the non-coronal effects are relatively weak, as shown in figure 3. Towards the outer mid-plane, the density decreases, and τ increases. A reasonable upper limit of τ is the inverse ELM frequency, the presence of large filaments may also reduce the effective τ. A more precise treatment requires time and position dependent calculations of plasma background and impurity state population rate equations. At this level of complexity, 2D effects like transport and flows should also be included, which will be present in 2D SOLPS calculations. In the following, time-independent calculations are used with a fixed non-coronal parameter.

The power out of the core plasma, P_{up}, is fed into the upper end of the flux bundle, located at the tokamak outer midplane.

$$q_{\parallel} = P_{up}/(2\pi R_{omp}\lambda_q sin(tan^{-1}(B_\theta/B_\phi))) \quad (1)$$

The denominator is the cross-section area of the flux bundle, A_{cross}. From the divertor entrance situated at the target distance L_{div} to the mid-plane, the narrow power width λ_q is supposed to be valid, which is about 2 mm in AUG at I_p= 1 MA and predicted to be slightly below 1 mm in ITER [7]. The power width λ_q derived from IR measurements at the target and the validity of Spitzer conductivity could recently be confirmed by Thomson scattering measurements of the T_e width in the outer midplane using the

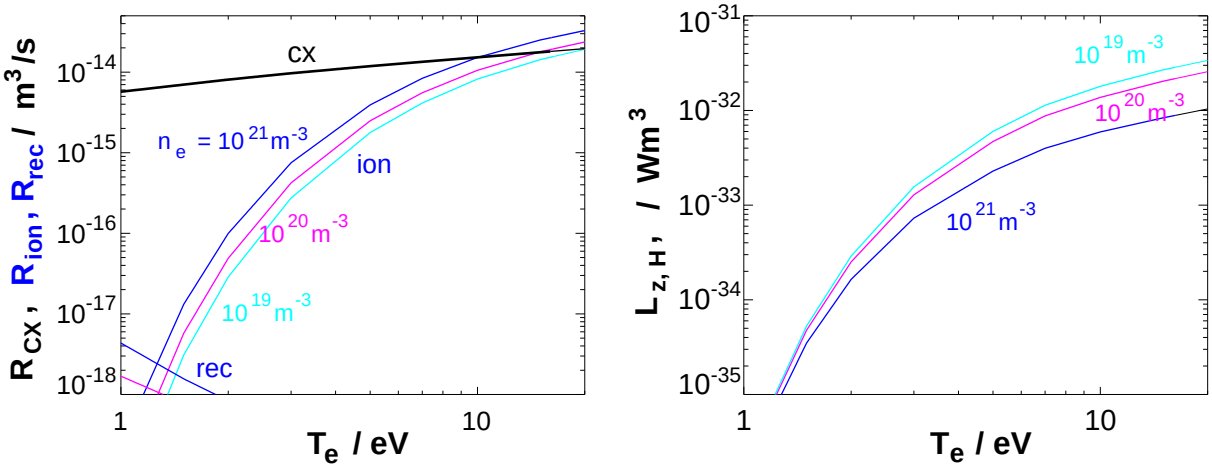

Figure 2. *Rate coefficients for ionization of and charge exchange of deuterium and power loss function L_z from line radiation taken from ADAS. R_{ion} and L_z depend on the electron density.*

relation $\lambda_q = \frac{2}{7}\lambda_{Te}$ [25]. At the target, a broadened power width λ_{int} is measured due to the effect of the power spreading S, via $\lambda_{int} \approx \lambda_q + 1.64S$ [22]. The broadening increases with decreasing electron temperature in the divertor region [26]. In the 1D-model, we use a step-wise increase of the power width from the value λ_q to λ_{int} at a distance of L_{div}= 5 m along the flux bundle from the target. The exact physics mechanism of the broadening are not fully understood so far. A corresponding enhancement of radial transport in the divertor region was required for the matching of midplane and target profiles in SOLPS modelling of detached AUG discharges [4].

The cross-sectional area of the flux bundle in the divertor region is typically a factor 15-20 (corresponding to 1/sin(pitch angle $\approx 3^o$) smaller than the wetted area at the target. Particle flux or power densities parallel to B have to be divided by this factor when compared to target measurements by Langmuir probes, IR thermography or spectroscopy along lines of sight aligned perpendicular to the target. Towards the mid-plane, A_{cross} is further reduced by the factor λ_q/λ_{int}, which we assume as 1/3 for typical conditions in this study. The temperature gradient follows from the heat flux and the thermal conductivity. Charge exchange and recombination are introduced as momentum loss terms, however, recombination is found to play a negligible role for the parameters of this study. Further general assumptions are $T_i = T_e$ and $n_e = n_i$, neglecting dilution by impurities, and $n_z = c_z n_e$, where c_z is the impurity concentration. The indices e,i, are sometimes retained to underline the species involved in the physics process. Temperatures and energies are given in [eV], otherwise SI units are used.

The neutral flux density $\Gamma_0 = n_0 v_0$ emerging from the target is taken from the boundary conditions for the electron temperature, $T_{e,tar}$, and the power to the target, P_{tar}, under the assumption of 100 % recycling, with the sheath energy transmission factor $\gamma = 8$ and sonic flow towards the target with Mach=1. The neutral deuterium flux from the target is divided into 2 velocity groups each carrying half the flux.

The first group has a velocity corresponding a neutral temperature of T_0= 5 eV, representing reflection of sheath accelerated ions and Franck-Condon neutrals. The neutral velocity along the flux bundle is assumed to be 1/4 of the mean thermal speed, $v_0 = 1/4\ (8/\pi\ eT_0/m_0)^{0.5}$. The second group is started at the plate with a velocity higher by a factor 10, representing neutrals entering the flux tube further upstream from the side. The results of the 1D calculations do not sensitively depend on the flux ratio of the two velocity classes.

Neutrals produced by volume recombination are added to Γ_0, ensuring that all ions lost are replaced by ionization events. This dislocation of neutrals (and of the energy carried by them) is regarded acceptable within this simple model.

$$\frac{\partial}{\partial x} n_0 = -R_{ion} n_e n_0 / \ v_0 \ + \ R_{rec} n_e n_i / \ v_0 \tag{2}$$

The charged particle flux towards the target is obtained by integration of the ionization source from the target following the continuity equation:

$$\frac{\partial}{\partial x}(nv) = R_{ion} n_e n_0 - R_{rec} n_e n_i \quad \rightarrow$$

$$n(x)v(x) = \ n_{tar} v_{tar} \ + \ \int_{x=0}^{x} (R_{ion} n_e n_0 - R_{rec} n_e n_i)\ dx' \tag{3}$$

This equation is used to calculate the plasma flow velocity v, which is negative since always directed towards the target within the presented model. The recombination rate contains radiative and 3-body recombination, therefore R_{rec} depends on T_e and n_e.

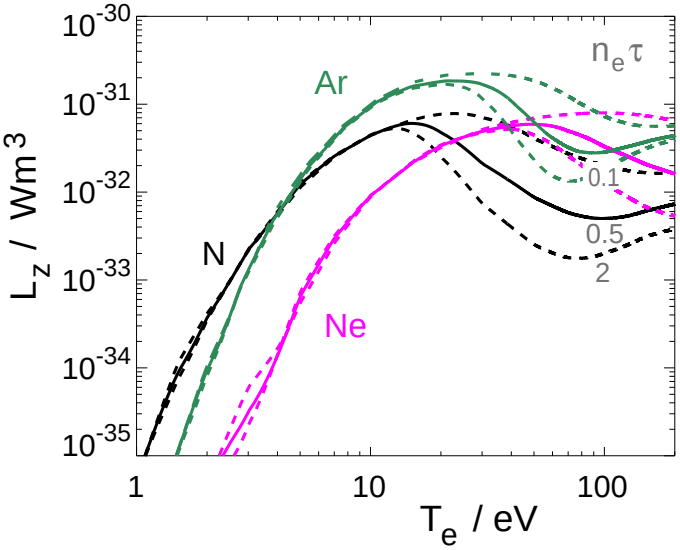

Figure 3. *Radiative loss functions calculated from ADAS for possible divertor seeding gases N, Ne, Ar and* $n_e = 1{\cdot}10^{20}\ m^{-3}$. *Solid lines have been calculated for the non-coronal parameter* $n_e\tau = 0.5$ *as used throughout this study, the upper and lower dashed lines for each species correspond to values* $n_e\tau = 0.2$ *and* $2 \cdot 10^{20}\ ms\ m^{-3}$.

Divergence of the parallel heat flux is caused by radiation, charge exchange and ionization losses. Impurity radiation loss functions are shown in figure 3. Since the

coordinate x starts at the target, the loss terms are added to the parallel heat flux, which rises in direction towards the mid-plane.

$$\frac{\partial q_{\parallel}}{\partial x} = \; n_e^2 c_z L_z(T_e) \; + eT_i R_{CX} n_i n_0 \; + eE_{ion} R_{ion} n_e n_0 - \frac{\partial q_{conv}}{\partial x} \tag{4}$$

The last term takes into account the convective heat flux, $q_{conv} = \; (5eTn + \frac{1}{2} m_i n v^2)v$, which has to be fed by the upstream $q_{\parallel}$. It is important for low T_e conditions, where the heat is transported mainly convectively. The influence of recombination on the energy balance has been omitted in eq. 4, since at not too low temperatures most of the recombination energy is radiated. The target boundary condition for the parallel heat flux is calculated from the target power taking the convected heat flux into account.

The heat flow causes a temperature drop along the flux bundle given by

$$q_{\parallel} = \; -\kappa_0 T_e^{5/2} \frac{\partial T_e}{\partial x} \approx \; -2390 \frac{J}{s \; m \; eV^{7/2}} \cdot Z_{eff}^{-0.3} T_e^{5/2} \frac{\partial T_e}{\partial x} \tag{5}$$

The term $Z_{eff}^{-0.3}$ approximates the reduction of the thermal conductivity with increasing Z_{eff} [27]. The upstream value of $q_{\parallel}$ obtained from 1D modelling starting at the target is related to the total power flux over the separatrix, P_{sep}. Assuming Mach=1 at the target / sheath entrance, the simplified momentum conservation can be written as [19]

$$\frac{\partial}{\partial x} \left(n(m_i v^2 + 2eT)\right) = \; -m_i v R_{CX} n_i n_0 \; - m_i v R_{rec} n_e n_i \tag{6}$$

With this ansatz, the momentum losses are maximised, a fractional momentum regain by the ionization of fast CX or recombined neutrals is neglected. By integrating Eq. 6 along the field line, the following expression for the electron density is obtained:

$$\begin{aligned} n_e(x) = {} & (m_i M^2 c_s^2 + 2eT)^{-1} \cdot (n_{e,tar}(m_i M_{tar}^2 c_{s,tar}^2 + 2eT_{tar}) \\ & - \int_{x=0}^{x} m_i M c_s (R_{CX} n_i n_0 \; + \; R_{rec} n_e n_i) \; dx') \end{aligned} \tag{7}$$

Here the Mach number has been introduced via, v= Mc_s with the thermal sound speed $c_s = \; (2eT/m_i)^{0.5}$.

The above equations are integrated starting from the target plates with a variable spatial step size, increasing from target to mid-plane. The reason is that at the target more robust boundary conditions can be set (see Chapter 12 in [19]). Starting from upstream would suffer from the experimental uncertainties of density and temperature at the separatrix. Consequently, the loss terms for momentum and the associated power loss are added as source terms. The divertor region is assumed to be the region up to a distance of L_{div} from the strike point measured along the target. L_{div}= 5 m (see figure 1) is used for default in AUG, and this value is kept also for machines with larger R. Radiation emerging from x $\leq$ L_{div} is counted as divertor radiation. The two major caveats of the 1D model should be pointed out here: first, there is no perpendicular neutral or plasma transport, and the plasma flow is restricted to the region close to the target which is accessible to neutrals starting from the target. Second, the step-wise variation of the power width along the flux tube is a crude model and the chosen distance of the step position from the target is quite uncertain due to the lack of physics understanding of its origin.

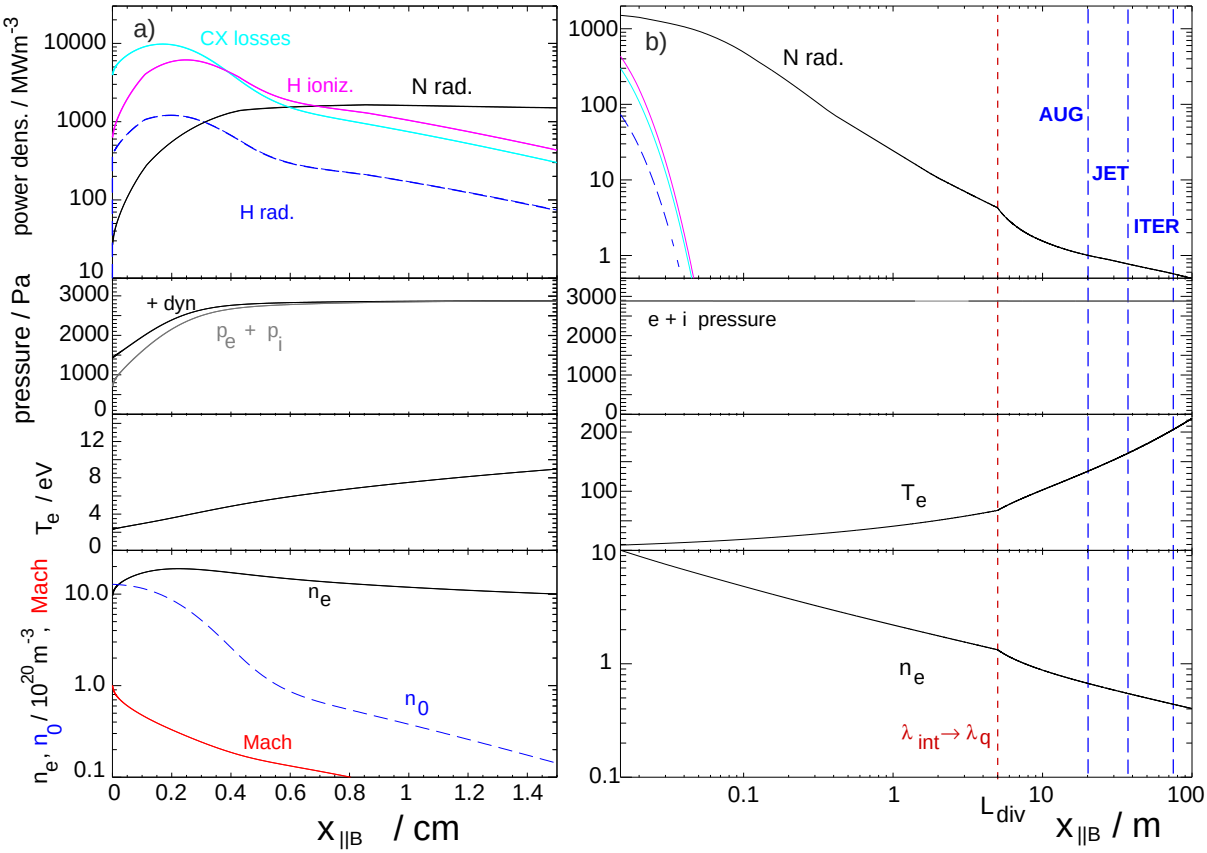

Figure 4. *a) Plasma parameters and radiative losses according to the 1D model close to the target and b) along the flux tube up to the midplane. The parameters correspond to semi-detached divertor conditions: divertor nitrogen concentration c_N=0.04, $T_{e,tar}$= 2.3 eV, power load of 2.3 MW/m^2, f_{mom}=0.5, neutral pressure p_0= 4.9 Pa. The power width λ is reduced from 5 mm to 2 mm at the divertor entrance L_{div}. Dashed vertical lines indicate the midplane for devices of different size. P_{up} is 4.7 MW for the AUG size (R= 1.65 m, L=20 m) and 27 MW for the case with R= 8.25 m, L= 100 m. Corresponding values of the separatrix power, P_{sep}, are 10.8 and 62 MW, respectively*

Figure 4 shows a 1D model calculation for typical conditions of this study with a momentum loss factor f_{mom}= 2 $T_{tar}n_{tar}$ / ($T_{up}n_{up}$)= 0.5 between target and mid-plane. Fully attached conditions would correspond to f_{mom}= 1 as a result of the Mach=1 boundary condition. Calculations along the field line are done up to 100 m, corresponding to 5 times the connection length from the outer divertor to the mid-plane in AUG, thus representing a machine of the size R= 8.25 m. For the geometry of the larger machines, indicated by vertical lines, negligible additional momentum loss occurs away from the target, therefore T_e rises in upstream direction due to the conductive heat flow and n_e drops due to momentum conservation. For identical target conditions, the larger device has a higher $T_{e,mid}$ and a smaller $n_{e,mid}$.

The step in power width from λ_{int} to λ_q is introduced under conservation of power and pressure (note that there is vanishing plasma flow at this position in the present

calculations, otherwise a pressure change would occur). As can be seen in figure 4, this causes a steeper T_e rise and n_e drop towards the midplane. Without the more narrow upstream width, the midplane separatrix density in AUG would be over-estimated by the 1D model. As another consequence, the radiated power density also decreases steeper, since L_z decreases with rising T_e for these conditions. The radiated power outside the divertor decreases even stronger, since the radiating volume outside the divertor is decreased by the step factor 3. On the target side of the ionization front, for low temperatures the energy transport gets predominantly convective, the parallel T_e flattens similar to experimental observations with divertor Thomson scattering in the DIII-D tokamak [28]. Figure 5 shows a summary of the input and output variables of the 1D model.

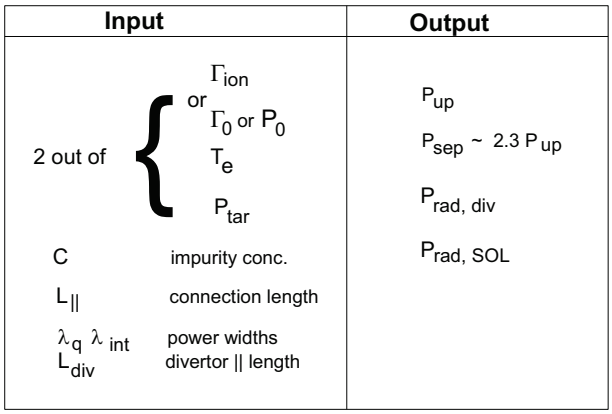

Figure 5. *Input and output variables of the 1D model. Ion flux / the neutral flux which is assumed to be equal, temperature and power are related by the sheath condition, i.e. the third quantity follows from each combination of two.*

3. Model calculations for ASDEX Upgrade experimental conditions

To reproduce realistic divertor conditions, input parameters to the model have to be adapted to measurements. Due to the calculation scheme starting at the target, boundary conditions are mainly set by the divertor diagnostics, like the ion saturation current, T_e and power flux density from Langmuir probe (LP) measurements. The latter are equivalent as long as derived from LPs, since the same sheath model as in the 1D model is used to derive the power flux from the LP measurement.

Validation or invalidation of the 1D model can mainly be done by comparison to the upstream heat flux from heating power and core radiated power or to upstream measurements of T_e or n_e in the outer midplane. Reasonable agreement is usually obtained, but the comparisons are hampered by uncertainties in the separatrix position by about $\pm$ 5 mm, which translate into a considerable uncertainty of $T_{e,sep}$ and also $n_{e,sep}$.

Another appropriate parameter for comparison with experiments is the divertor neutral pressure p_0, which is an important engineering parameter for the divertor

performance and is also used to parametrise the detachment behaviour in SOLPS calculations in preparation of ITER [29] [30]. p_0 can be related to the neutral flux density via $p_0 = \Gamma_0 \cdot sin(\alpha)/\ (1.55 \cdot 10^{23} m^{-2} s^{-1})$ [Pa]. α is the angle of incidence of the field line at the target, taken to be 3 degree in this study, typical for AUG and also considered as reasonable engineering limit for a DEMO device [31]. The numerical factor converts the flux density at the target into a molecular pressure at room temperature. For the partially detached conditions considered here, neutrals emerging from the target have are reasonable chance to reach the region below the roof baffle, and vice versa. The pumped neutral flux is significantly smaller than the target recycling flux, therefore the neutral fluxes to and from the roof baffle have to be of similar magnitude. In ASDEX Upgrade, ion fluxes from LP measurements close to the outer strike point and neutral flux measurements by ionization gauges and a baratron in the region below the roof baffle show similar values at the onset of detachment.

4. Parameter scans with 1D model calculations

While the results of the 1D model calculations are possibly too simplified for a quantitative comparison with experiments, correct trends should be given and extrapolations should be possible. The most important parameter is the upstream power, P_{up}, which should be compared to the total experimental power over the separatrix, P_{sep}. For given target parameters and neutral density, adding of impurities in the model causes an increase of the upstream power. This power is required to compensate the additional radiative losses. The momentum loss in the 1D model is closely connected to the electron temperature in front of the target, in line with experimental findings [32]. The reason is the growing importance of charge exchange versus ionization and heat conduction at low temperatures. The effect of impurity species or heat flux on the onset temperature for detachment is very weak, as shown in figure 6.

An important parameter for the power exhaust is the power width λ_{int}. The 1D model implies that the plasma parameters T_e, n_e, parallel heat flux etc. stay identical if λ_{int} and the target power are varied by the same factor (maintaining flux densities), upstream power and radiated powers then scale with the same factor.

4.1. Model parameter variations for semi-detached conditions

The simple model allows extensive parameter scans and thus the investigation of main parameter dependences of divertor radiation on plasma (boundary) conditions and impurity species. We concentrate here on the working point of partial detachment, for which an experimental scaling had recently been derived for nitrogen seeded H-mode conditions in the closed, vertical outer divertor of the ASDEX Upgrade tokamak [18]:

$$q_{det} = P_{sep}/R\ \ (p_0\ +\ 18 p_{0,N})^{-1}\ \times\ 1.3\ Pa\ m\ /MW \tag{8}$$

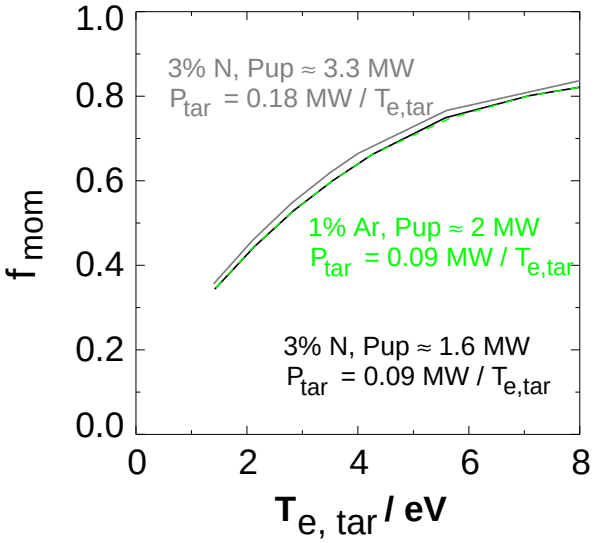

Figure 6. *Momentum loss factor versus electron temperature at the target from different 1D model runs. Parameter variation is done by scaling target T_e and target power with the same factor (see figure), this keeps the upstream power constant within ± 10 per cent due to the decreasing degree of detachment with rising T_e. $c_N = 0.03$ with two different power levels, $c_{Ar} = 0.01$. Since P_{tar} and T_{tar} are scanned proportionately, the particle fluxes and hence the neutral pressure stay constant during the scan, namely $p_0 = 1.7$ Pa for the two low power scans and $p_0 = 3.5$ Pa for the high power scan with N.*

q_{det} is here a detachment qualifier which takes the value of one at the partially detached conditions considered here. In the experimental analysis, the nitrogen concentration c_N in the divertor was approximated by the ratio of the D and N valve fluxes under approximately stationary conditions. The factor 18 is the relative radiative efficiency of nitrogen, $f_N = 18$. The choice of the onset point of partial detachment has the advantage that it can be determined robustly from the experiment via the vanishing of the thermoelectric divertor current [18], as well as well-defined in the model via the momentum loss factor.

In the following, we reconcile eq. 8 with 1D model calculations as shown in figure 4. For this, the parameters of eq. 8 have to be matched to those introduced in section 2. Since the upstream power $P_{up} = q_{\|} \cdot A_{cross}$ in the 1D model regards only the heat flux towards the outer divertor, the total power over the separatrix, P_{sep}, is higher. P_{up} represents only a fraction 1-1/e of the power to the outer divertor, in addition the power to the inner divertor and to the main chamber wall have to be taken into account. Assuming, somewhat arbitrarily, an in-out power asymmetry of 1:2, the power fraction f_{out} to the outer target defined by $P_{sep} = f_{out}\ P_{up}$ is $1.5/(1 - 1/e)) = 2.37$. We use the corresponding factor $f_{out} = 2.3$ obtained by a comparison of the 1D model calculations with the experiment, which is consistent with the simple consideration above. The relative radiation efficiency $f_N = 18$ of equation 8 is used for the selection of the appropriate non-coronal parameter, which has been set to $n_e\tau = 0.5 \cdot 10^{20}$ ms m^{-3} in

the 1D calculations to obtain $f_N = 18$ there. The same value of the non-coronal parameter $n_e\tau$ is used for the 1D calculations for neon and argon. The impurity concentration used in the 1D modelling, c_z, is associated with the ratio of the deuterium and impurity valve fluxes under quasi-stationary conditions, where the pumped fluxes in the divertor must correspond to the gas input fluxes. There is some uncertainty related to this assumption because the impurity concentration may vary over the divertor region, but a direct measurement of c_z is not available in the divertor plasma. c_z is supposed to decrease further upstream due to impurity enrichment in the divertor. The point of semi-detachment in the modelling is defined by the static momentum loss factor $f_{mom} = 0.5$. This is to some degree an arbitray choice. It is motivated by the fact that momentum losses should be important, but not the dominant process at the target, because the simple 1D model loses validity when neutral transport becomes more important.

Figure 7 shows the 1D modeling data versus the extended formula 8, as given below in equation 9. Calculations for neon and argon were done exactly as those for nitrogen, their corresponding radiative efficiencies $f_{Ne} = 45$ and $f_{Ar} = 90$ were derived by fitting the 1D calculations to equation 9. The relative values of f_N, f_{Ne}, f_{Ar} describe the divertor radiation level for a given concentration, or the inverse concentrations which are required to obtain detachment for certain experimental conditions. The absolute numbers denote, with somewhat higher uncertainty, the relative capabilities of the impurities to dissipate power in comparison to deuterium. The variation of the target temperature for constant $f_{mom} = 0.5$ is quite small (between 2.3 and 2.6 eV) for all data in figure 7, again showing that the electron temperature is the governing parameter for the onset of detachment at least within the 1D model.

The good ordering of the data in figure 7a suggests that the functional behavior chosen to describe P_{sep}/R for the detachment point is appropriate, albeit better, but more complicated fits may be obtainable. Figure 7b shows the deviations from the fit function for the radiation-weighted impurity concentrations $f_z c_z$. Reduced upstream power or divertor radiation is seen at high values of $f_z c_z$. This is explained by the saturation of the divertor radiation already expected from analytic calculations [21] [14]. For pure D plasmas or small $c_z f_z$, equation 9 somewhat overestimates the losses compared to 1D modelling. For intermediate impurity concentrations, the combined effect of D and seed impurities is well described by the double-linear dependence on the weighted pressures.

Finally, the size dependence as predicted by the 1D model is investigated. Since we use fixed target boundary conditions, a deviation from the P/R dependence may arise from the additional upstream radiation caused by the flux tube length L increasing $L \propto R$. Figure 8 shows the variation of $P_{sep}/R = 2.3\ P_{up}/R$ with R via the varied flux tube length by scaling the AUG parameters to $L = 20/1.65 \cdot R$. Divertor radiation by the seed impurity is the dominant heat spreading process for the current conditions, also in line with EDGE2D-EIRENE 2D modelling of JET divertor detachment by nitrogen seeding [5]. A slightly positive size effect of the SOL radiation is observed in the 1D model with fixed divertor length L_{div} (figure 8a), depending on the impurity species. With the

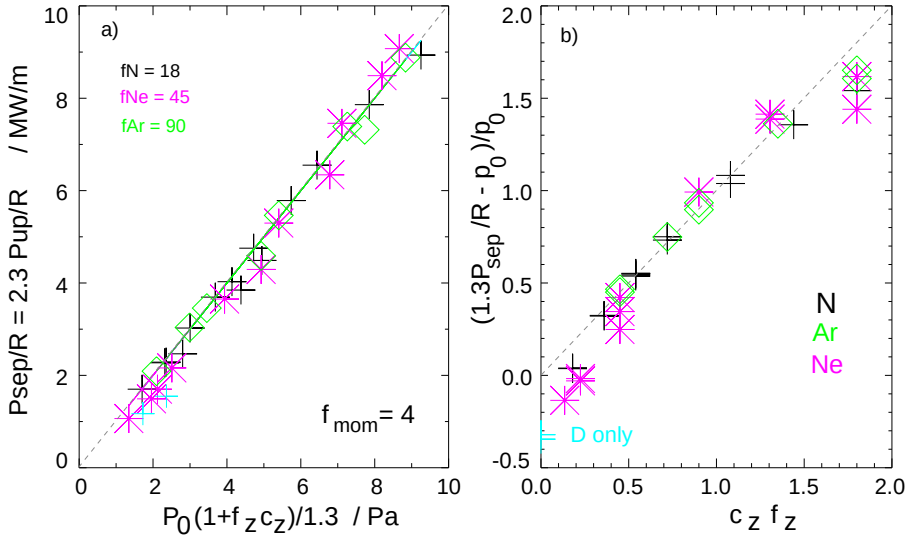

Figure 7. *a) 1D model calculations for different values of p_0, c_N, target power and a fixed static momentum loss factor f_{mom}= 0.5, representing partially detached conditions in the AUG tokamak, with major radius R= 1.65 m. The target heat load was varied between 0.8 and 2.4 MW/m^2, not counting recombination energy, T_e at the target was adjusted to obtain f_{mom}= 0.5 by variation of $T_{e,target}$ between 2.3 and 2.6 eV. Due to this low variation, p_0 changes about proportional to the target heat load. Variations of c_z resulted mainly in a change of the upstream power. Power width λ_{int}= 5 mm, reduced by 1/3 at 5 m distance from the target. The dashed lines represent the scaling equation 9. b) Normalized contribution of the weighted impurities to the power dissipation $c_z f_z$ versus the scaling prediction, highlighting the deviations from the scaling predictions. At high values of $c_z f_z$, a saturation of the radiation losses is observed. With very low impurity concentration, the scaling over-predicts P_{sep}.*

divertor length rising ∝R (figure 8b), the divertor radiation rises stronger with machine size due to the increasing volume.

In summary, the following equation is obtained for the partially detached operation point for an arbitrary sized device with a closed divertor target and impurity seeding:

$$P_{sep}/R|_{det.point} = \frac{1}{1.3} p_0 (1 + f_z c_z) \cdot (\lambda_{int}/0.005m) \cdot (R/1.65m)^{r_z} \qquad (9)$$

$$[MW/m,\ Pa,\ m]$$

Element	Nitrogen	Neon	Argon
f_z	18	45	90
r_z (L_{div} =5 m)	0.038	0.033	0.043
r_z (L_{div} =5 m · R/1.65 m)	0.1	0.19	0.11

Table 1. *Coefficients for equation 9, f_z is the relative efficiency for detachment achievement compared to deuterium. r_z is the weak exponent for the size dependence of detachment onset, caused by the increase of upstream radiation with field line length for fixed L_{div} and mainly by increased divertor radiation for $L_{div} \propto R$.*

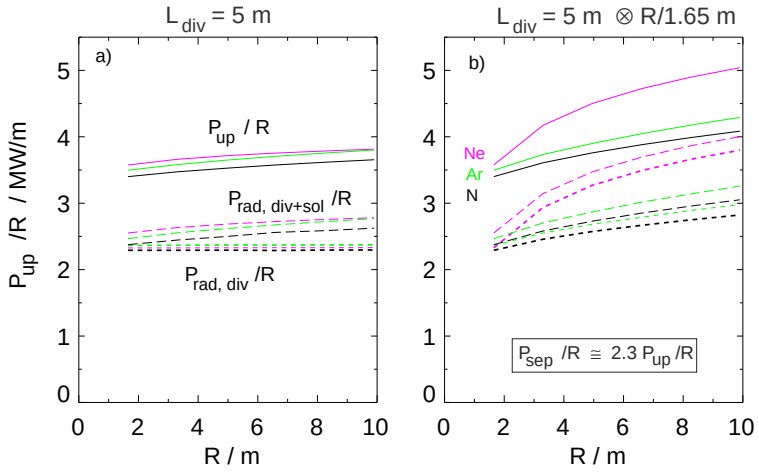

Figure 8. *Machine size dependence of the normalized upstream power P_{up}/R for N, Ne and Ar seeding and a fixed momentum loss factor f_{mom}= 0.5 . Impurity concentrations are fixed, c_N= 0.06, c_{Ne}=0.024, c_{Ar}=0.012 . Note that $P_{sep}/R \approx 2.3\ P_{up}/R$. Target heat flux 2.3 MW/m^2, T_e =2.33 eV, p_0= 4.9 Pa. $P_{rad,div}$ is the radiated power integrated along the flux bundle from target to L_{div}, $P_{rad,div+sol}$ the radiation along the whole flux bundle. a) λ_{int}= 5 mm, step to 5/3 mm at z=5 m for all R. b) λ_{int}= 5 mm, step to 5/3 mm at z=5 m · R / 1.65 m. The larger divertor parallel length L_{div} leads to an increase of the divertor radiation with R.*

The inclusion of λ_{int} follows directly from the 1D model equations. Coefficients f_z and r_z are given in table 2, where r_z depends on the chosen model for the divertor λ broadening. The weakly positive size dependence is mainly caused by SOL and divertor radiation depending on the position of the step in λ. Note that equation 9 with the coefficients given in table 2 are valid for the chosen values of L_{div} and the lambda step by a factor 3 at the position L_{div}.

4.2. Predictions for larger, future devices

Due to the matching against AUG divertor conditions, most reliable extrapolation is expected for devices with a similar divertor geometry, divertor density and width λ_{int}. This is e.g. in reasonable approximation the case for ITER. An upper operational limit is expected for the divertor neutral flux due to the occurrence of the H-mode density limit [8]. In AUG, so far a pressure of 5 Pa has been achieved without significant confinement degradation, and no pressure limit was hit for high power seeded conditions. Experiments are ongoing to increase the pressure at highest P_{sep}/R. For a future high field device [33], a smaller power width λ_{int} is expected [7], but this may be compensated by a higher divertor pressure being permitted by a higher H-mode density limit.

Evaluating eq 9, the following predictions for the required impurity concentration for the achievement of partial detachment at P_{sep}/R= 15 MW/m and 10 Pa neutral divertor pressure in an ITER-sized device with R=6.2 m and λ_{int}= 0.005 m are obtained: c_N= 0.047, c_{Ne}= 0.019, c_{Ar}= 0.0094. For half the neutral pressure, p_0= 5 Pa, the

required impurity concentrations are about a factor 3 higher, which would not be acceptable for ITER or a DEMO. For the case that the broadened divertor region extends in length with machine size, the predicted impurity concentrations to invoke partial detachment at 10 Pa neutral pressure are reduced: c_N= 0.0393, c_{Ne}= 0.0115, c_{Ar}= 0.0076. The higher Z elements appear favorable regarding plasma fuel dilution, but their resulting core radiation is problematic at least for ITER, where P_{sep} without core seed impurity radiation is not far above the L-H threshold power. For DEMO, the core radiation problem will be relaxed since P_{sep} will be much higher than P_{L-H}.

5. Conclusions

Required impurity concentrations and neutral flux densities for semi-detached operation of a standard closed divertor have been calculated by 1D modelling. Effects of inner divertor and private flux region, which cannot be treated with this simple model, have been incorporated by a factor f_{out}=2.3 relating the power over the separatrix, P_{sep}, and the upstream power towards the outer divertor, P_{up}. The appropriate value of the non-coronal parameter $n_e \cdot \tau$ has been adapted by comparing the 1D model calculations to the experimental detachment point with nitrogen seeding. Detachment induced by Ne and Ar seeding has been determined using the same procedure, however, a direct comparison with experimental data is not possible due to the not well known radiation fraction by Ne and Ar inside the separatrix. The values of both fitting parameters are compatible to the results of simple physics considerations. Some caveats of the procedure used in this paper have to be mentioned. The presented 1D model calculations are time-independent. In reality, divertor radiation shows pronounced temporal variations due to ELMs and fluctuations which are induced by spatial variations of the emitting zones, in particular in the inner divertor/X-point region [13]. While these time dependent effects may be at least partially captured by matching the non-coronal parameter to the experimental conditions, time-dependent modelling would be a next step of refinement. A direct measurement of the seed impurity concentration c_z in the divertor plasma would also be very helpful for a quantitative analysis and hence also the prediction of divertor radiation.

The quite high values of c_z in the divertor required for high power dissipation will not be acceptable in the core of a burning device, either due to too strong fuel dilution (N, Ne) or core radiation (Ar). Therefore, enrichment of the impurity in the divertor is required, which lowers the corresponding core concentrations [34]. Improvements of the standard divertor may be possible towards higher enrichment values, and future studies both by modelling and experiments are recommended. The use of argon in a high power device like DEMO may be feasible even without large enrichment, since here - in contrast to ITER - a high core radiation level is permitted due to a high P_{heat}/P_{LH} and is also required for the reduction of P_{sep}.

6. Acknowledgements

This work has been carried out within the framework of the EUROfusion Consortium and has received funding from the Euratom research and training programme 2014-2018 under grant agreement number 633053. The views and opinions expressed herein do not necessarily reflect those of the European Commission.

7. References

[1] WISCHMEIER, M. et al., Journal of Nuclear Materials **415** (2011) S523.
[2] CANIK, J. et al., J. Nucl. Mater. **463** (2015) 569.
[3] WISCHMEIER, M. et al., J. Nucl. Mater. **463** (2015) 22.
[4] REIMOLD, F. et al., J. Nucl. Mater. **463** (2015) 128.
[5] JAERVINEN, A. et al., J. Nucl. Mater. **463** (2015) 135.
[6] EICH, T. et al., Phys. Rev. Lett. **107** (2011) 215001.
[7] EICH, T. et al., Nuclear Fusion **53** (2013) 093031.
[8] BERNERT, M. et al., Plasma Physics and Controlled Fusion **57** (2015) 014038.
[9] REIMOLD, F. et al., Nuclear Fusion **55** (2015) 033004.
[10] AHO-MANTILA, L. et al., Nuclear Fusion **52** (2012) 103006.
[11] POTZEL, S. et al., J. Nucl. Mater. **463** (2015) 541.
[12] BERNERT, M. et al., Review of Scientific Instruments **85** (2014) 033503.
[13] POTZEL, S. et al., Nuclear Fusion **54** (2014) 013001.
[14] KALLENBACH, A. et al., Plasma Physics and Controlled Fusion **55** (2013) 124041.
[15] KUKUSHKIN, A. et al., J. Nucl. Mater. **463** (2015) 586.
[16] ZOHM, H. et al., Nucl. Fusion **53** (2013) 073019.
[17] STANGEBY, P. C. and LEONARD, A. W., Nucl. Fusion **51** (2011) 063001.
[18] KALLENBACH, A. et al., Nuclear Fusion **55** (2015) 053026.
[19] STANGEBY, P., *The Plasma Boundary of Magnetic Fusion Devices*, Institute of Physics Publishing, Bristol and Philadelphia, 2000.
[20] LACKNER, K. and SCHNEIDER, R., Fusion Eng. and Design **22** (1993) 107.
[21] POST, D. et al., Phys. Plasmas **2** (1995) 2328.
[22] MAKOWSKI, M. et al., Phys. Plasmas **19** (2012) 056122.
[23] ADAS, www.adas.ac.uk/manual.php .
[24] CAROLAN, P. and PIOTROWICZ, V., Plasma Physics **25** (1983) 1065.
[25] SUN, H. J. et al., Plasma Physics and Controlled Fusion **57** (2015) 125011.
[26] SCARABOSIO, A. et al., Journal of Nuclear Materials **463** (2015) 49.
[27] GOLDSTON, R., Nucl. Fusion **52** (2012) 013009.
[28] LEONARD, A. et al., Nucl. Fusion **52** (2012) 063015.
[29] KUKUSHKIN, A. and PACHER, H., Plasma Phys. Controlled Fusion **44** (2002) 931.
[30] KUKUSHKIN, A. et al., J. Nucl. Mater. **438** (2013) S203.
[31] WENNINGER, R. et al., Nucl. Fusion **54** (2014) 114003.
[32] LIPSCHULTZ, B. et al., Fusion Science and Technology **51** (2007) 369.
[33] LABOMBARD, B. et al., Nucl. Fusion **55** (2015) 053020.
[34] BOSCH, H.-S. et al., Plasma Physics and Controlled Fusion **39** (1997) 1771.